RCS Scatterer Extraction Using Apriori Target Information

J.T. Mayhan

Lincoln Laboratory

MASSACHUSETTS INSTITUTE OF TECHNOLOGY

LEXINGTON, MASSACHUSETTS

The ESC Public Affairs Office has reviewed this report, and it is releasable to the National Technical Information Service, where it will be available to the general public, including foreign nationals.

This technical report has been reviewed and is approved for publication.

FOR THE COMMANDER
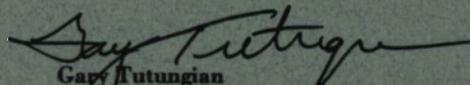
Gary Tutungian
Administrative Contracting Officer
Plans and Programs Directorate
Contracted Support Management

Massachusetts Institute of Technology
Lincoln Laboratory

RCS Scatterer Extraction Using Apriori Target Information

J.T. Mayhan
Group 34

Lexington   Massachusetts

ACKNOWLEDGMENTS

ABSTRACT

Target component feature extraction is an area of considerable importance to the Ballistic Missile Defense (BMD) community. In particular, extracting essential target features from measurement data on targets of interest leads to potential target identification. The extracted component features correspond to a numerical characterization of the Geometrical Theory of Diffraction (GTD) diffraction coefficient and can also be used to develop a computationally efficient, measurement based RCS signature prediction model. A key attribute of the resulting computational model is that the measured RCS is directly incorporated into the computational model.

An essential ingredient in forming a measurements-based signature model valid over a wide range of frequencies and angles is the ability to map the field measurement data (2 dimensional) onto a component-based three-dimensional (3D) geometry. To accomplish this, 3D characterization of the target scattering components is required. Typically, this 3D characterization of the scatterer locations is obtained by forming a 3D image of the target, and extracting the dominant scattering centers. In this paper we extend the novel formulation for 3D radar imaging of Inverse Synthetic Aperture Radar (ISAR) sparse-angle data using high-resolution spectral estimation theory presented in a previous paper (Ref 1) to the special case where one has apriori information about the target geometry.

For some applications one has apriori information about the target geometry—for example in processing static range data or in processing flight-test field data on "known" targets. In this paper, we develop a methodology which incorporates this known surface geometry constraint to generate a 3D ISAR image identifying the principal scatterers contributing to the target radar cross-section. The methodology uses only a sequence of single snapshot data, from which key features on the target can be readily extracted. The technique eliminates the need for a range-Doppler correlator required to track the motion of any specific scatterer. This is accomplished by hypothesizing a given target surface constraint (3D), and mapping sequential 2D range-Doppler location estimates onto this surface. The process is adaptive, as the assumed geometry is modified as appropriate (e.g., for intelligence related apriori information) to match the data. When applied to the sequence of high-resolution snapshots obtained using the direct spectral estimate obtained from sequential blocks of data, it presents a computationally efficient way of generating a high-resolution 3D image from which the dominant scattering centers on the given surface constraint are identified and characterized.

TABLE OF CONTENTS

LIST OF ILLUSTRATIONS

1. INTRODUCTION

Target component feature extraction is an area of considerable importance to the Ballistic Missile Defense (BMD) community. In particular, extracting essential target features from measurement data on targets of interest leads to potential target identification. The extracted component features can also be used to develop a computationally efficient, measurement-based RCS signature prediction model. A key attribute of the resulting model is that the measured RCS is directly incorporated into the computational model.

An essential ingredient in forming a measurements-based signature model valid over a wide range of frequencies and angles is the ability to map the field measurement data, 2 dimensional (2D), onto a component-based three-dimensional (3D) geometry. To accomplish this, 3D characterization of the target scattering components is required. Typically, this 3D characterization of the scatterer locations is obtained by forming a 3D image of the target, and extracting the dominant scattering centers. In this paper we extend the novel formulation for 3D radar imaging of Inverse Synthetic Aperture Radar (ISAR) data using high-resolution spectral estimation theory presented in a previous paper (Ref 1) to the special case where one has some apriori information about the target geometry.

In previous papers, we developed a novel formulation of the 3D imaging problem based on a simple mathematical representation for the 2D to 3D image transformation, which processes a sequence of independent 2D high-resolution snapshots of the target to generate the 3D image points. The formulation uses modern 2D spectral estimation techniques to enhance the resolution obtained using conventional correlation imaging techniques. This new technique offers several advantages:

1. Provides for a direct 3D estimate (vs. back projection to a 3D target grid matrix) of the location of the dominant scattering centers, having enhanced resolution both in range and cross-range relative to conventional imaging.

2. Provides a direct estimate of each scatterer amplitude and phase as a function of aspect-angle to the target.

3. Produces a 3D image with only a minimum number of independent snapshots, where each snapshot represents a high-resolution range-Doppler image at a known aspect angle. Because of the snapshot nature of the technique, it is particularly applicable to 3D imaging of sectors of sparse-angle data, for which the sidelobes of the correlation imaging integral become high.

4. Gracefully reduces to a range only (e.g. wideband radar, low pulse repetition frequency (PRF)) and Doppler only (e.g. narrowband radar, high PRF) 3D imaging capability.

5. By implementing a range-Doppler correlation tracker on a sequence of pulses, one can isolate the 3D motion of any specific scatterer using the simple 2D to 3D mapping developed later in

1

the paper, and extract the scatterer amplitude and phase as a function of time. Using this scatterer response, combined with the 3D scatterer locations extracted from the 3D image, one can directly reconstruct the actual scattering measurements using a simple point scatter model based on the Geometrical Theory of Diffraction (GTD). Correlating the extracted GTD based diffraction coefficients to hypothesized characteristics of the scatterer response provides the potential of enhanced scatterer typing and identification.

For some applications one has apriori information about the target geometry – For example in processing static range data or in processing flight-test field data on known targets. Of prime interest in this case is identification of the dominant scattering centers on the target, with the intent to form a computationally efficient, measurements based, signature model of the target. In this report, we develop a methodology which incorporates this known surface geometry constraint to generate a 3D ISAR image identifying the principal scatterers contributing to the target radar cross-section. The methodology uses only a sequence of single snapshots of data from which key features on the target can be readily extracted. The technique eliminates the need for a range-Doppler correlator required to track any specific scatterer. This is accomplished by hypothesizing a given target surface constraint (3D), and mapping sequential 2D range-Doppler location estimates onto this surface. The process is adaptive, as the assumed geometry is modified as appropriate to fit the measured data. When applied to the sequence of high-resolution snapshots obtained using the direct spectral estimate obtained from sequential blocks of data, it presents a computationally efficient way of generating a high-resolution 3D image where the dominant scattering centers on the given surface constraint are identified and characterized.

Because the technique provides an independent estimate of the location of each scattering center, and a separate aspect angle and frequency dependence for this scatterer, when we refer to an "image" in this paper, we consider only the *positions* of the scatterers in target centered space. A conventional image also provides a measure of the average intensity at these locations, usually plotted on a color intensity scale on the 3D grid matrix. However, for real targets, this complex amplitude varies considerably with look angle, and we chose to delineate this variation separately. It is in fact this component characterization which leads to the measurements based signature model of the target.

2

2. 2-DIMENSIONAL ALL-POLE SIGNAL MODELING (REVIEW)

A general development of the 3 D signal model characterizing the high-frequency field scattered from a specific target using the Geometrical Theory of Diffraction (GTD) and its relationship to 2D, all-pole signal modeling techniques was developed in Reference 1. For completeness, we repeat this development in this section. We assume a target centered coordinate system as illustrated in Figure 1.
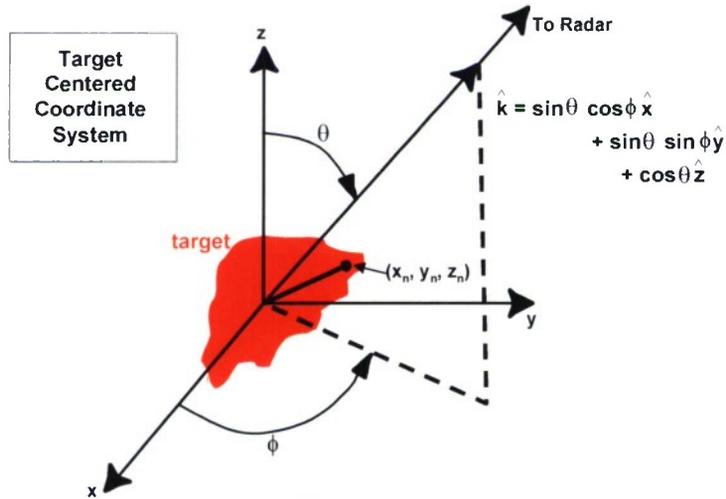
Figure 1

Figure 1. Coordinate System and Notation

Standard spherical coordinates θ, ϕ characterize the look-angle to the radar, which is determined by the unit vector $\hat{k}$ given by

$$\hat{k} = \sin\theta\cos\phi\,\hat{x} + \sin\theta\sin\phi\,\hat{y} + \cos\theta\,\hat{z} \tag{1}$$

where the notation "$\wedge$" denotes a "unit vector." The target coordinates are defined relative to the origin of this system, and an arbitrary scattering point on the target is denoted as (x_n, y_n, z_n). We assume the motion is known, so that in the target centered reference frame, the look angle of the radar changes parametrically with time; i.e., $\theta = \theta(t)$, $\phi = \phi(t)$.

3

Using the Geometrical Theory of Diffraction (GTD) the field E_n scattered from an arbitrary point located at (x_n, y_n, z_n) is given

$$E_n \sim D_n (f, \theta, \phi) e^{-j \frac{4\pi f}{c} \hat{k} \cdot r_n} \tag{2}$$

where $c = 3 \times 10^8$ m/s, f denotes frequency, $\underline{r}_n$ denotes the vector location of (x_n, y_n, z_n) and D_n (f, θ, ϕ) is the well-known scattering diffraction coefficient introduced by Keller [Ref. 2]. In a generalized sense, the scattering coefficient D_n characterizes a broad class of scattering features. It will be seen later that it corresponds directly to the amplitude and phase extracted from measurement data using 2D all-pole spectral estimation techniques.

In general, D_n by itself is a complex function whose frequency and angle variation is considerably slower than the total phase variation in (2). Thus a snapshot of data provides information only on the local variation of D_n when viewed as a wide angle, broadband function.

Wide-angle characterization of D_n is accomplished by processing a "block" of pulses consistent with changes in $\theta(t)$, $\phi(t)$. Eq (2) is rigorously valid in the frequency domain, for a single pulse. For the time scales considered here, the time variable "t" represents "pulse-to-pulse" changes in the radar return. Since the changes in θ, ϕ are not directly radar observables, the radar return pulses are processed as a function of frequency and time. In frequency-time space, the measurement of E_n can be expressed in the form:

$$E_n \sim D_n (f, t) e^{-j \psi_n (f, t)} \tag{3}$$

where $\psi_n (f, t)$ and $D_n (f, t)$ are implicitly a function of $\hat{k}$ and $\underline{r}_n$ according to

$$\psi_n (f, t) = \frac{4\pi f}{c} \hat{k}(t) \cdot \underline{r}_n$$
$$D_n (f, t) = D_n (f, \hat{k} \cdot \underline{r}_n) \tag{4}$$

Equations (3) and (4) provide projections defined relative to a 3D signal model. However, the radar observables (f, t) comprise a 2D space. Thus a mapping from 2D radar observable space to 3D target centered space (i.e.; x_n, y_n, z_n) is required for 3D imaging.

Consider the local approximations of ψ_n and D_n over frequency and time. From the concept of all-pole modeling, D_n (f,t) can be locally approximated as having an exponential behavior, i.e.,

$$D_n (f, t) \sim D_{0_n} e^{-\alpha_n f} e^{-\beta_n t} \tag{5}$$

where α_n and β_n characterize the localized exponential approximation and D_{0n} is a complex constant. This local approximation is particularly convenient for using 2D all-pole modeling spectral-estimation techniques, for which the poles characterizing the signal model have an exponential behavior with complex exponent. The phase behavior ψ_n (f, t) is somewhat more complicated. Consider two special cases:

a. *Fixed* θ_0, ϕ_0. Vary f $= f_0 + k\Delta f$, $k = 1,\dots K$

Then we can expand ψ_n (f, t_0) in the form

$$\psi_n (f, t_0) = \psi_n (f_0, t_0) + \left(\frac{\partial \psi_n}{\partial f} \Delta f \right) k \tag{6}$$

where t_0 corresponds to $\theta_0 = \theta (t_0)$, $\phi_0, = \phi (t_0)$.

b. *Fixed* f_0. Vary t $= t_0 + q \Delta t$, $q = 1,\dots, Q$

For this case we can expand ψ_n (f_0, t) in the form

$$\psi_n (f_0, t) \sim \psi_n (f_0, t_0) + \left(\frac{\partial \psi_n}{\partial t} \Delta t \right) q \tag{7}$$

If Δf and Δt are small enough, Eqs (6) and (7) can be combined to form a 2D all-pole signal model valid for linear imaging (e.g., as for the conventional range-Doppler image). In this case, the field E_n (f, t) becomes a function of the discrete 2D sequence, E_n (k, q), which can be written in the form

$$E_n(k, q) = D_{0n} s_n^k p_n^q \tag{8}$$

where the complex poles s_n and p_n are given by

$$s_n = e^{-\Delta f\left[\alpha_n + j\left(\frac{\partial \psi_n}{\partial f}\right)\right]} \tag{9}$$

$$p_n = e^{-\Delta t\left[\beta_n + j\left(\frac{\partial \psi_n}{\partial t}\right)\right]} \tag{10}$$

A conventional linear image could then be obtained using a weighted 2D Fourier transform on Eq (8). However enhanced resolution is realized when the poles s_n, p_n are determined from a 2D pole estimation algorithm applied to the measurement data set. Once the pole pairs (s_n, p_n) are determined, the complex amplitude D_{on} can be extracted using a "least squares" fit of a sum of poles, each weighted by D_{on} in the form of Eq (8), to the measured data set.

Figure 2 illustrates the methodology used for sequential processing of a block of uncompressed radar data pulses. The poles s_n and p_n are extracted from the composite scattered field data matrix $E(k, q)$ and converted to range and range rate space using (9) and (10). We obtain

$$\ln s_n = -\left(\alpha_n + j\frac{\partial \psi_n}{\partial f}\right)\Delta f$$

$$\ln p_n = -\left(\beta_n + j\frac{\partial \psi_n}{\partial t}\right)\Delta t \tag{11}$$

Using Eq (4), we obtain

$$\frac{\partial \psi_n}{\partial f} = \frac{4\pi}{c}\hat{k}\cdot\underline{r}_n$$

$$\frac{\partial \psi_n}{\partial t} = \frac{4\pi f}{c}\hat{k}\cdot\underline{\dot{r}}_n, \tag{12}$$

6

where we define $\dot{\hat{k}} \equiv d\hat{k}/dt$. Substituting Eq (12) into (11), we obtain the desired mapping:

$$R_n \equiv \hat{k} \cdot \underline{r}_n = -\frac{c}{4\pi \Delta f} \text{Im} (\ln s_n) \tag{13}$$

$$\dot{R}_n \equiv \dot{\hat{k}} \cdot \underline{r}_n = -\frac{\lambda}{4\pi \Delta t} \text{Im} (\ln p_n) \tag{14}$$

where we define (R_n, $\dot{R}_n$) to be the range, range rate observables corresponding to (x_n, y_n, z_n) and Im (z) denotes the "imaginary part" of the complex variable z. The complex amplitude D_n associated with each spectral component (scatterer) is computed by the 2 D spectral estimation algorithm. The sequence $\{R_n, \dot{R}_n, D_n\}_q$ can then be used for image interpretation and component extraction and characterization.

7

3. SEQUENTIAL BLOCK PROCESSING FOR COMPONENT EXTRACTION AND CHARACTERIZATION (REVIEW)

The sequence $\left\{R_n, \dot{R}_n, D_n\right\}_q$ where n denotes the nth scatterer present in the data at time snapshot $t = t_q$, provides a sequential characterization of the target scattering components and RCS as a function of time. We now show how this sequence can be used for image interpretation and component extraction and characterization.
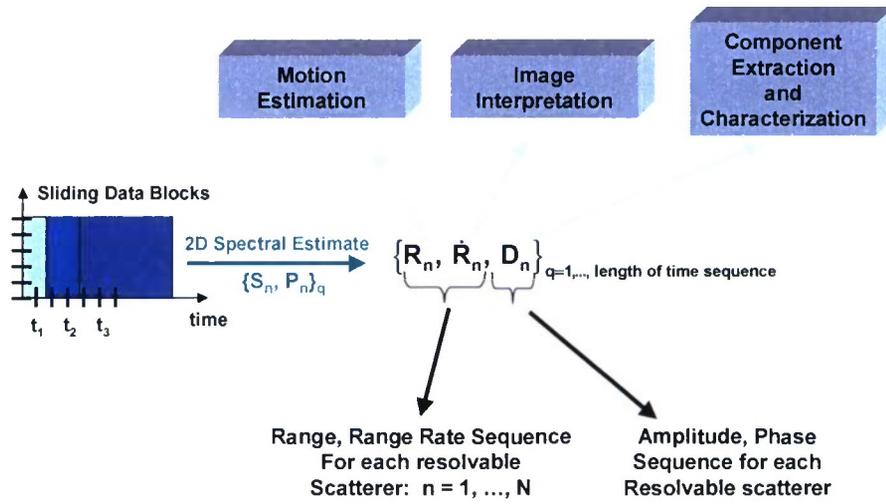
Figure 2

Figure 2. Sequential Block Processing

Figure 3 illustrates a typical result for a single data block using simulated data on a spinning cylinder with "fins" attached at one end. Two specific 2D spectral estimation algorithms have been developed, one based on ESPRIT processing techniques (Ref. 3) and the other based on a state-space formulation (Refs 4,5). The resulting $(R_n, \dot{R}_n)$ estimates are overlaid on a conventional weighted Fourier Transform based range-Doppler image. The $\otimes$ marked points on the image represent the direct estimate of the scatterer locations to within the accuracy of the Cramer-Rao bound obtained by applying ESPRIT directly to the data block. Processing these high-resolution ($R_n, \dot{R}_n$) estimates provide several advantages over processing the conventional image:

9

1. The estimate of (R, $\dot{R}$) for each scatterer is direct – i.e. it need not be inferred from the image. The resultant extraction provides a computationally efficient numerical sequence for further processing to determine motion and component characterization.

2. The resolution and accuracy achieved closely approaches the Cramer-Rao bound for each scatterer location.

3. The amplitude and phase of each scatterer is a direct output of the spectral estimate, and need not be inferred from the image (such as when using the so-called "clean" extraction algorithm applied to a conventional DFT-based range-Doppler image). For example, the 3D image generated can be constructed using only scatterers above a certain amplitude, thus eliminating "noisy" or unimportant scatterers.
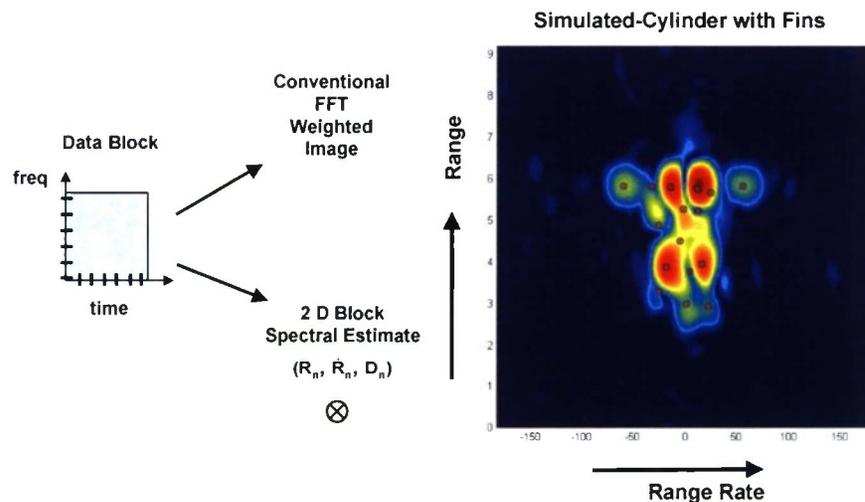

Figure 3

Figure 3. High-resolution Block Processing vs. Conventional DFT Image

10

4. HIGH-RESOLUTION 3D IMAGING USING CUMULATIVE SNAPSHOTS

The technique developed in Reference [1] using cumulative snapshots to form a 3D image will be briefly summarized in this section. It is most useful for simpler targets characterized by a small number ($\lesssim 10$) of scatterers). Each pulse return is uncompressed and de-weighted to obtain the frequency domain representation of the scattered field for that particular look angle. A 2D spectral estimation algorithm is applied to a block sequence of pulses to estimate s_n, p_n, and D_{0n}. A R, $\dot{R}$ correlator/smoother is implemented to track these poles in R, $\dot{R}$ space, sequentially sliding (at fixed jump intervals) a block of pulses through the measurement data set. Eq (13) and (14) are then applied sequentially to a number of snapshots to develop an estimate of the scattering points (x_n, y_n, z_n). To illustrate this process mathematically, we express the transformation defined by (13) and (14) in matrix form:

$$\underline{\underline{T}}_{q_1} \cdot \begin{bmatrix} x_n \\ y_n \\ z_n \end{bmatrix} = \begin{bmatrix} R_n \\ \dot{R}_n \end{bmatrix}_{q_1} \tag{15}$$

where $\underline{\underline{T}}$ is a 2 x 3 transformation matrix given by

$$\underline{\underline{T}} = \begin{bmatrix} \hat{k} \\ \dot{\hat{k}} \end{bmatrix} \tag{16}$$

where $\hat{k}$ and $\dot{\hat{k}}$ are expressed as row vectors, and Eq (15) defines the mapping at $t = tq_1$. It is readily shown that

$$\dot{\hat{k}} = \left[\dot{\theta}\, \hat{\theta} + \dot{\phi} \sin \theta\, \hat{\phi} \right] \tag{17}$$

We can accumulate these equations for two snapshots at tq_1 and tq_2 in the form

11

$$\begin{bmatrix} \underline{\underline{T}}_{q_1} \\[2ex] \underline{\underline{T}}_{q_2} \end{bmatrix} \cdot \begin{pmatrix} x_n \\ y_n \\ z_n \end{pmatrix} = \begin{bmatrix} \begin{pmatrix} R_n \\ \dot{R}_n \end{pmatrix}_{q_1} \\[3ex] \begin{pmatrix} R_n \\ \dot{R}_n \end{pmatrix}_{q_2} \end{bmatrix} \tag{18}$$

As additional snapshots are obtained, these equations are added to (18), which is then solved in a least squares sense for the scattering coordinates (x_n, y_n, z_n).

Note that the accumulation of snapshots emphasizes the importance of a good R, $\dot{R}$ tracker, particularly in low signal-to-noise ratio environments. It is imperative in Eq (18) that the sequence of R_n, $\dot{R}_n$ estimates correspond to the same physical scatterer located at (x_n, y_n, z_n). For the results presented in Ref 1, we used a simple "nearest neighbor" tracking algorithm in R, Rdot space to track the motion of the scatterers.

In the next section, we develop a simple version of (18) not requiring an accumulation of snapshots, by adding a third equation, obtained by imposing a surface constraint to the two equations defined by Eq (15).

5. 3D SNAPSHOT IMAGING USING A SURFACE CONSTRAINT – DEVELOPMENT

Expand the transformation matrix $\underline{\underline{T}}$ into a more general form defined by

$$\underline{\underline{T}} = \begin{bmatrix} T_{11} & T_{12} & T_{13} \\ T_{21} & T_{22} & T_{23} \end{bmatrix} \tag{19}$$

Thus, each scatterer (x_n, y_n, z_n) on the surface S must satisfy the condition

$$T_{11}\, x_n + T_{12}\, y_n + T_{13}\, z_n = R_n \tag{20}$$

$$T_{21}\, x_n + T_{22}\, y_n + T_{23}\, z_n = \dot{R}_n \tag{21}$$

If the surface S is known (or hypothesized), then an additional equation completing (20) and (21) above can be obtained by requiring

$$S\,(x_n, y_n, z_n) = 0 \tag{22}$$

where, in general, $S\,(x, y, z) = 0$ describes the target surface geometry. Imposing the condition Eq (22) on (20) and (21) provides a direct set of generally independent equations which define a (x_n, y_n, z_n) scatterer position using a single snapshot of data. The tradeoff that we will elaborate on later is the existence of several types of ambiguous solutions, which map to the surface but do not correspond to physical scatterers on the target. We address this topic further in section 6.

Two simple cases will be considered in this section for example purposes: a cone and a cylinder. These provide for a simple, direct solution for constructing a 3D image directly from the field measurement, which can be "thresholded" by prefiltering on the amplitudes $|D_n|$ associated with each

13

scatterer. Although simplistic in nature, the examples lead to a quantitative understanding to the application of the technique. For the two cases considered, we have

    a.   Cylinder (Radius a)

$$S\,(x,\,y,\,z) \;=\; x^2 + y^2 - a^2 = 0 \tag{23}$$

    b.   Cone (Cone half-angle θ_c)

$$S\,(x,\,y,\,z) \;=\; z\text{-}z_b \;+\; \operatorname{ctn}\theta_c \cdot \sqrt{x^2 + y^2} \;= 0 \tag{24}$$

where "a" is the cylinder radius and z_b denotes a surface bias (shift) used to align the cone with the data.

Eqs (20) – (22) although nonlinear in nature, can be solved exactly for these two simple surface constraints. For both cases, Eqs (20) and (21) can be solved to express x_n and y_n as functions of z_n and written in the form

$$y_n = a_1\, z_n \;+\; b_1 \tag{25}$$

$$x_n = a_2\, z_n \;+\; b_2 \tag{26}$$

$$a_1 = \frac{T_{13}\,T_{21}\;-\;T_{11}\,T_{23}}{\Delta} \tag{27}$$

14

$$b_1 = -\frac{T_{21} R_1 - T_{11} \dot{R}_1}{\Delta} \qquad (28)$$

$$a_2 = -\frac{T_{13} T_{22} - T_{12} T_{23}}{\Delta} \qquad (29)$$

$$b_2 = \frac{R_1 T_{22} - T_{12} \dot{R}_1}{\Delta} \qquad (30)$$

and

$$\Delta = T_{11} T_{22} - T_{12} T_{21} \qquad (31)$$

Using (25) and (26) for x_n and y_n in either (23) or (24) defining S (x, y, z) produces a quadratic equation for z_n. Once z_n is determined, x_n and y_n can be computed from (25) and (26). Note that since (23) and (24) are quadratic in form, two solutions for z_n will be generated. For the simple cases considered here, the correct solution is readily determined. However in the more general case, these ambiguous solutions must be filtered out as discussed in Section 6.

5.1 A SIMPLE EXAMPLE (SIMULATION)

To illustrate the technique, consider the simulation considered in Ref [1], and illustrated in Figure 4. The target consists of a spherical tipped, conical model of a re-entry vehicle (RV) of length = 1.6 m, having 4 antenna ports located at 90°–roll intervals and having a flat base. Each antenna port was simulated to be a constant amplitude scatterer independent of roll and 5 dB reduced from the nose. We simulated wideband pulses (using standard Physical Theory of Diffraction (PTD) codes to compute the net scatter vs. frequency, and a hamming weighted Fourier Transform over frequency to generate the compressed pulse shapes) received by an X-band sensor for motion defined by a spinning target without coning. Figure 4 illustrates the RV geometry and target orientation for $\theta_0 = 40°$. An X-band bandwidth of 1 GHz is used for example purposes. Data is processed for a variety of snapshots taken over a 360° roll cycle. Also shown in Figure 4 are the composite, weighted pulse shapes received at the sensor over the full 360° roll cycle, where the radar line of sight to the target is from right to left – i.e., the nose is roughly 10 dB larger than the base. Note that the antenna ports are clearly resolvable from the nose and base. For

15

any given roll angle, two antenna ports are visible in the same range resolution cell, resulting in a pulse-pulse variation of the pulse return in the RV midsection due to the interaction of the two antenna port scatterers. Since the nose and base of the target are roll symmetric, the pulse returns from these scatterers are insensitive to time for constant aspect angle and hence these scatterers produce zero Doppler return. Thus they correspond to so-called "slipping scatterers."
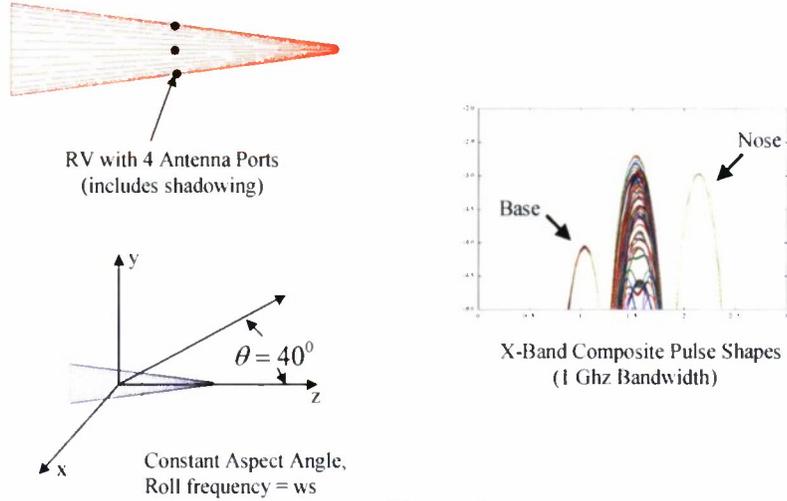

Figure 4

Figure 4. Constant Aspect Angle Imaging (Spinning RV with Shadowed Antenna Ports)

Figure 5 illustrates the $\left\{R_n, \dot{R}_n\right\}_q$ sequence extracted from the data over one complete roll cycle of the target, and the resulting 3D RV "image" reproduced from Ref 1 using the (x_n, y_n, z_n) computed by correlating the scatterers and accumulating snapshots according to Eq (18). Note that a multi-aspect wide-angle image is required for complete target imaging because of shadowing. For the pure spinning motion considered, the base of the target presents zero Doppler to the radar line of sight, and thus appears as a slipping scatterer. For the image illustrated, we modify the conventional image of the base return as a slipping scatterer by moving the base slipping scatterer to its projected (x_n, y_n, z_n) location assuming an a priori known base diameter. This model-based approach to imaging slipping scatterers is often used when additional data on the target from known sources or other wide-angle aspect angle observations is available. Alternately, if motion change in the orthogonal direction is available, e.g., if the RV is "coning" as well as spinning, additional orthogonal snapshots could be added to the image processing.

Figure 6 illustrates the 3D image generated using the conical surface constraint defined by Eq (24) for $\theta_c = 7.3^\circ$. Gaps in the slipping scatterer image appear because the noise inherent in the $\dot{R}$ poles

16

that occur as each antenna port approaches the shadow region were filtered out. Note also that the base slipping scatterer is automatically projected to the proper position on the cone surface, and is consistent with the model-based projection used in Figure 5 assuming an apriori known base diameter.

Figure 7 illustrates the sensitivity of the images to cone angle θ_c, as indicative of using the cone angle as a parameter to "focus" the image when the cone-angle might not be apriori-known exactly. Clearly best results occur for $\theta_c = 7.3^\circ$, where the resulting variance in antenna port locations is due to the variance in $\dot{R}_n$ estimate shown in Figure 5.
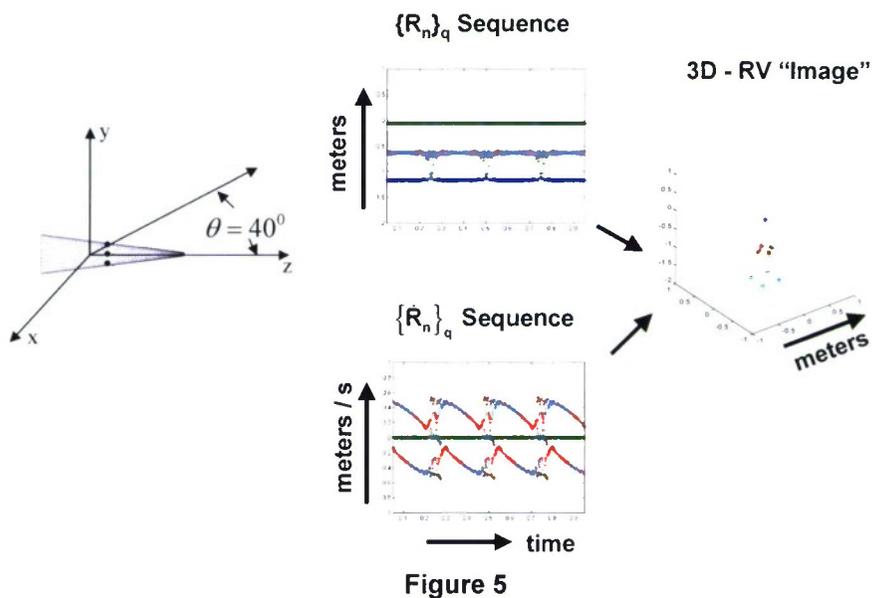
Figure 5

Figure 5. Cumulative Block Processing to 3D-Target "Image"

Antenna Ports
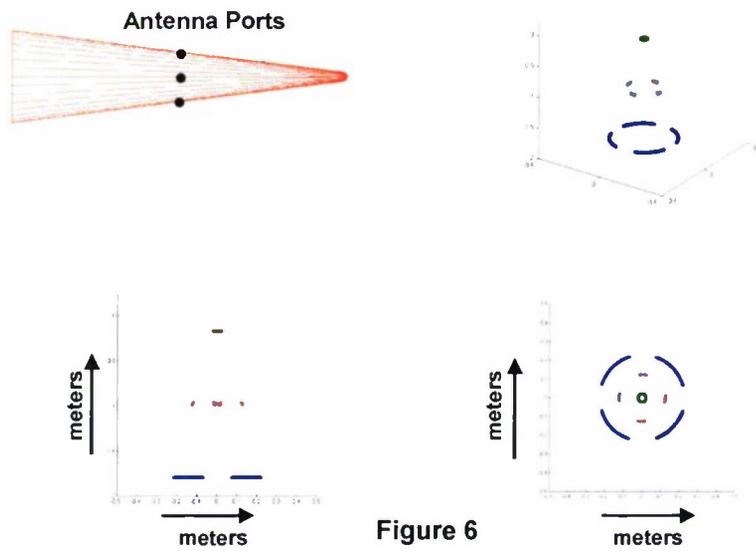
Figure 6

Figure 6. 3D Snapshot Image with Sequential Conical Surface Constraint

Antenna Ports

Top View

$\theta_c = 8°$

$\Phi_c = 8°$

$\Phi_c = 6.6°$
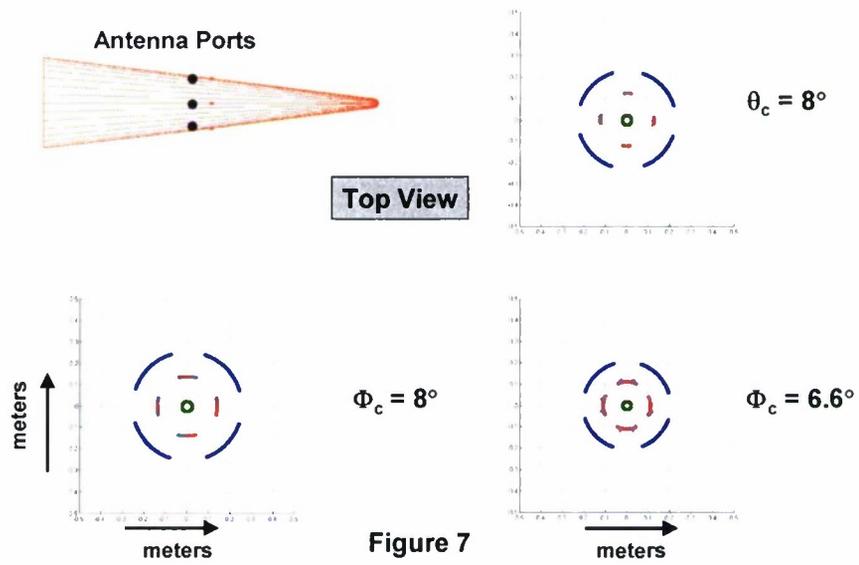
Figure 7

Figure 7. Image Defocusing vs. Error in Cone Angle (Top View)

6. A GENERAL "CAD-MODEL" SURFACE CONSTRAINT

The examples of the previous section demonstrate the utility of applying the surface constraint to a simple conical RV-like surface geometry. However the cone and cylindrical surfaces are usually too simplistic to be useful for application to complex targets, and a more general approach is required. We now develop this more general approach by considering the surface $S(x,y,z) = 0$ to be defined numerically at a fixed number of grid points

$$S(x_p, y_p, z_p) = 0, p = 1,\ldots,N_g \tag{32}$$

where N_g denotes the total number of grid points defining the target surface. Consider, for example, a simplistic model of a missile rocket-body consisting of a finite cylinder having four equally spaced fins at the rear. A point-wise numerical representation of this surface is illustrated in Figure 8, showing a 3D, top and side view. (Note the x, y scales in Fig. 8 have been enlarged for clarity). Because of the similarities of this type of surface characterization to a computer-aided-design (CAD) model of the target, we adopt that nomenclature, recognizing that as defined here the model might not be suitable for input to other numerical electromagnetic computation codes. In fact one useful interpretation of the point-wise characterization of the surface useful in solving Eqs (20), (21) and (32) numerically is to view each point as a potential scatterer. The required density of the surface grid is then determined by the resolution of the sensor (in range and cross-range, given by, respectively, c/FBW and λ/FBW, where FBW is the fractional bandwidth of the sensor – i.e., $FBW = BW/f_0$, where BW is the actual bandwidth (Hz) and f_0 the operating frequency).
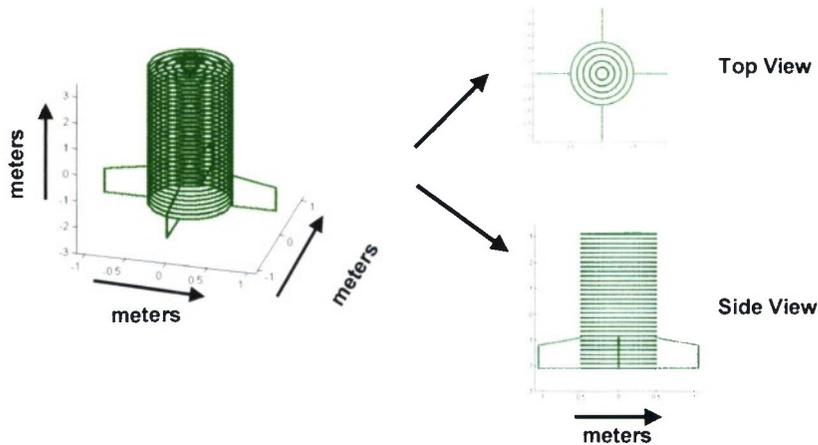

Figure 8. Rocket Body CAD Model for Simulation

19

The technique we use to solve Eqs (20, (21) and (32) is "hypothesis-test" based. For a given incidence angle (θ, ϕ), the scattering from the target is characterized by N pole pairs (converted to range, range rate using Eqs (13) and (14)), $\{R_n, \dot{R}_n\}$, $n = 1, \ldots, N$. In effect we will test each pair $(R_n, \dot{R}_n)$ corresponding to a given angle to check if it emanates from a particular point on the grid surface. The result usually corresponds to a physical scattering center and several ambiguous solutions (i.e., the point on the body is consistent with Eqs (20), (21) and (32), but is not one of the scattering centers contributing to the scattered field). We then apply a series of "ambiguity filters" to this solution, leading to the desired solution set $\{x_n, y_n, z_n\}$. This process is repeated for each incidence angle, and the resultant point-set corresponds to the dominant scattering centers on the target. When superimposed on the CAD model, they appear as an "image" of point-scatterer locations.

Quantitively, the process is described in the steps below:

4. Since most ballistic targets are nearly axially symmetric, it is useful to sort the grid matrix $\{x_g, y_g, z_g\}$ in increasing z_g; i.e. we assume

$$z_g = \text{sort}\,[z_g] \tag{33}$$

where $z_g(1) \leq z_g \ldots \leq z_g(N_g)$, and relabel x_g and y_g accordingly. This allows one to identify the front or rear of the target by its location in the ordered z_g string.

5. Consider now the set $\{R_n, \dot{R}_n\}$ characterizing the scattering at a specific angle (θ, ϕ). Assume that the scattering associated with each pair emanates from z_{gp}, where the subscript p denotes p[th] grid point. If this hypothesis were true, then the corresponding (x, y, z) scatterer coordinates would be given by (x_n, y_n, z_{gp}), where x_n and y_n are determined from

$$\begin{pmatrix} x_n \\ y_n \end{pmatrix} = T_{xy}^{-1}\, T_z\, z_{gp} - T_{xy}^{-1} \begin{pmatrix} R_n \\ \dot{R}_n \end{pmatrix} \tag{34}$$

and T_{xy} and T_z are defined as

$$T_{xy} = \begin{pmatrix} T_{11} & T_{12} \\ T_{21} & T_{22} \end{pmatrix}; \quad T_z = \begin{pmatrix} T_{13} \\ T_{23} \end{pmatrix} \tag{35}$$

To check the hypothesis, we compare the point $\left(x_n, y_n, z_{gp}\right)$ to see if it actually lies on the grid surface, according to an error tolerance ε_T:

$$|(x_g - x_n)^2 + (y_g - y_n)^2|^{1/2} < \varepsilon_T \tag{36}$$

If (36) is satisfied, we admit the point (x_n, y_n, z_{gp}) as a possible scattering center.

6. Repeat Step 2 for each grid point z_{gp}, $p = 1, \dots N_g$ and store the collection of possible scattering centers.

7. Apply a series of ambiguity filters to the initial data set $\{x_n, y_n, z_n\}$. These filters are developed in the following section.

6.1 SCATTERING MECHANISMS AND AMBIGUITY FILTERS

There are several physical mechanisms for which ambiguous scattering centers can occur using the above methodology. Some of these are:

a. "Shadowing"

b. Component to Component Coupling

c. Slipping Scatterers

d. CAD Model Surface Tolerances

We now develop appropriate "Ambiguity Filters" to eliminate these ambiguous solutions. We note that the specific filters to use are strongly target (surface) dependent, and those discussed here are focused on the cylinder-fin surface example considered. The mechanisms however are generally applicable to any specific target.

6.1.1 Shadowing

For the simple cone and cylinder examples considered in Section 5, multiple roots inherent to the quadratic analytic solution developed in Section 5 lead to a scatterer located in the shadow region. In fact, although not developed here, it is possible to find closed form expressions for (x_n, y_n, z_n) for the cylindrical constraint (23) for the case $\dot{\theta} = 0$, and demonstrate the presence of one of the quadratic roots occurring in the shadowed region. The same effect will be true for the more general case of the cylinder-fin CAD example.

A simple check can be imposed to filter out this ambiguous shadowed solution. Denote the candidate scatterer point as (x_n, y_n, z_n). The scatterer lies in the cylinder shadowed region whenever

$$\hat{k} \cdot (x_n, y_n, 0) < 0 \tag{37}$$

Eq (37) is strictly true for an infinite cylinder. For a finite cylinder, scatterers on the visible truncated top or bottom cylinder surface are not shadowed. Thus we apply (37) only to grid points $z_g < z_c$, where z_c is the height coordinate of the visible cylindrical cap.

6.1.2   Component to Component Coupling

For targets that have some components having large radial dimensions (e.g., fins), scattering from the outer surface can lead to an ambiguous scatterer projected to a smaller radial diameter surface (e.g., cylinder). Figure 9 illustrates this effect for the fin-cylinder surface geometry. (Note, the fins are only sparsely populated with grid points in this example). A side-view and top view clearly shows how scatterers having the same $(R, \dot{R})$ pairs resulting from fin scattering can project to the smaller diameter cylindrical surface. Thus, a fin-cylinder coupling ambiguity filter is required (Note, to emphasize this effect in Figure 9, we have chosen the error tolerance parameter ε_T in Eq (36) abnormally large).

It is easy to define the mathematical condition for this effect to occur. Denote (x_1, y_1, z_1) to be the true fin scatterer location and (x_2, y_2, z_2) the ambiguous scatterer location. These two points satisfy the common constraint

$$T_{xy} \begin{pmatrix} x_1 \\ y_1 \end{pmatrix} + T_z z_1 = T_{xy} \begin{pmatrix} x_2 \\ y_2 \end{pmatrix} + T_z z_2 = \begin{pmatrix} R_n \\ \dot{R}_n \end{pmatrix} \tag{38}$$
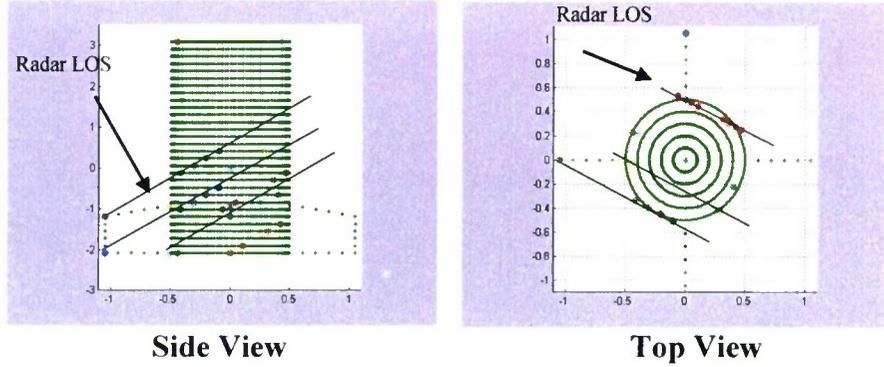
Figure 9. Ambiguous Scatterer Location

For the filter design, apply (38) to the condition that $(x_1, y_1, z_1,)$ is on a fin. When this occurs, positions (x_2, y_2, z_g) where z_g is an arbitrary grid position, must satisfy

$$\begin{pmatrix} x_2 \\ y_2 \end{pmatrix} = \begin{pmatrix} x_1 \\ y_1 \end{pmatrix} + T_{xy}^{-1} \, T_z \, (z_1 - z_g) \tag{39}$$

We simply apply (39) for every grid point z_g and filter out those points lying on the grid cylindrical surface.

6.1.3   Slipping Scatterers

Slipping scatterers are unique in the sense that they exhibit no Doppler with change in roll angle (ϕ). Thus, for $\dot{\theta} = 0$, $\dot{R} = 0$ for a slipping scatterer. Hence by definition it is an axially symmetric scatterer over the region for which $\dot{\phi} = 0$. The ambiguities generated for a slipping scatterer are typically in the shadow-region, and are filtered out by this filter. However, for the finite cylinder, the back-side scattering from the truncated top of the cylinder (shadowed for the infinite cylinder) is clearly visible to the radar when the aspect angle is less than 90°. The ambiguity associated with this "back-side" slipping scatterer is in the visible region, and still another filter is required. For this case, since it is unique, we simply compute its location and eliminate the point. To compute its position, we apply (38) assuming

23

(x_1, y_1, z_1) is the back-side slipping location and (x_2, y_2, z_2) is the visible region ambiguity. To compute z_2, we set $\phi = 0$, (by symmetry, for a slipping scatterer) for which $x_1 = -a$, $y_1 = 0$ and $z_1 = z_c$, where "a" is the cylinder radius and z_c is defined previously. For the ambiguity, $x_2 = + a$, $y_z = 0$. Then z_2 is given by

$$z_2 = z_c - 2a \tan\theta \tag{40}$$

The x_2, y_2 locations are the mirror images of the back-side slipping scatterer, i.e.

$$x_2 = a \cos \phi, \; y_2 = a \sin \phi \tag{41}$$

For the filter, we eliminate this point for each (θ, ϕ) when the cylinder back side "cap" is illuminated.

6.1.4   CAD Model Surface Tolerances

We note in the methodology presented, the "surface tolerance" parameter ε_T defined by Eq (36) is key to determining when a hypothesized scatterer lies on the surface. Typically, if ε_T is chosen too large, multiple ambiguities occur. This is illustrated in Figure 9, where we have deliberately chosen ε_T large. Ideally, ε_T is chosen on the order of the grid-spacing size. Clearly, there is a trade-off here. If ε_T is chosen too small, and the grid spacing is large, no scattering centers will be detected. For our purposes, ε_T is chosen somewhat empirically. for the surface geometry considered.

24

7. CYLINDER – FIN TARGET SIMULATION

In this section, we simulate the back-scattered field from a cylinder-fin type ballistic target using standard Physical Theory of Diffraction (PTD) type codes, and develop a CAD numerical surface model to illustrate the methodology developed in Section 6. We assume sensor parameters identical to those for the simulation in Section 5.1. Figure 10 illustrates the missile body cylinder-fin geometry used, as well as the dynamical motion parameters used to characterize a spinning (f_s= spin frequency), precessing (f_p = precession frequency) motion, where $f_s >> f_p$ and $T_p = 1/f_p$, $T_s= 1/f_s$. Figure 11 illustrates the example motion converted to (θ, ϕ) coordinates, and a range-time intensity plot over roughly 2 precession cycles. The sequence $\left\{ R_n, \dot{R}_n, D_n \right\}_{t = t_1...t_q}$ was extracted using sliding data blocks as described in Section 3.

The resulting sequence for $(R_n, \dot{R}_n)$ over the time interval [0.3, 0.5] seconds is illustrated in Figure 12, and the sequence for $|D_n|$ in Figure 13. Over this particular time interval, the radar illuminates the top portion of the cylinder. As can be seen from Figure 11, the aspect angle to the target, over this time interval, gradually decreases from ~100 degrees, through 90° (broadside) and up to the 60° minimum aspect angle determined by the assumed precession motion. Thus the observed range extension of the target increases as a function of time (over this interval) to a maximum, and then begins to decrease as θ increases out of minimum precession angle.
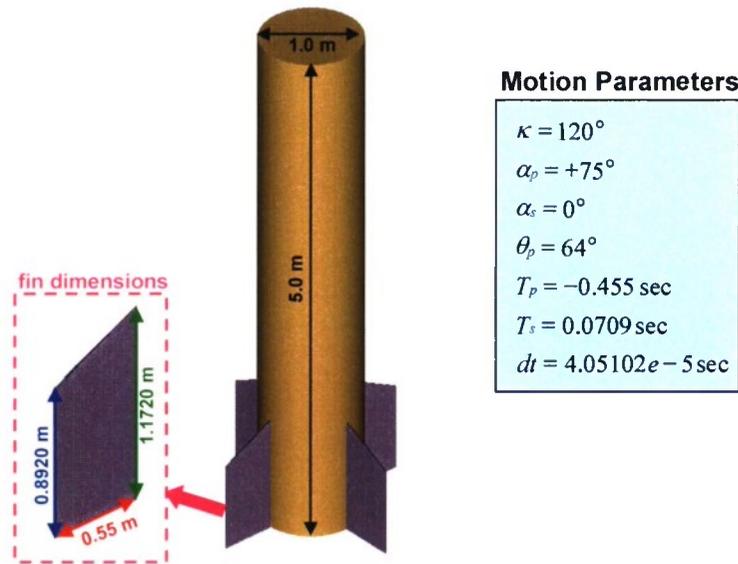

*Figure 10. Rocket-Body—CAD Model Simulation*

25
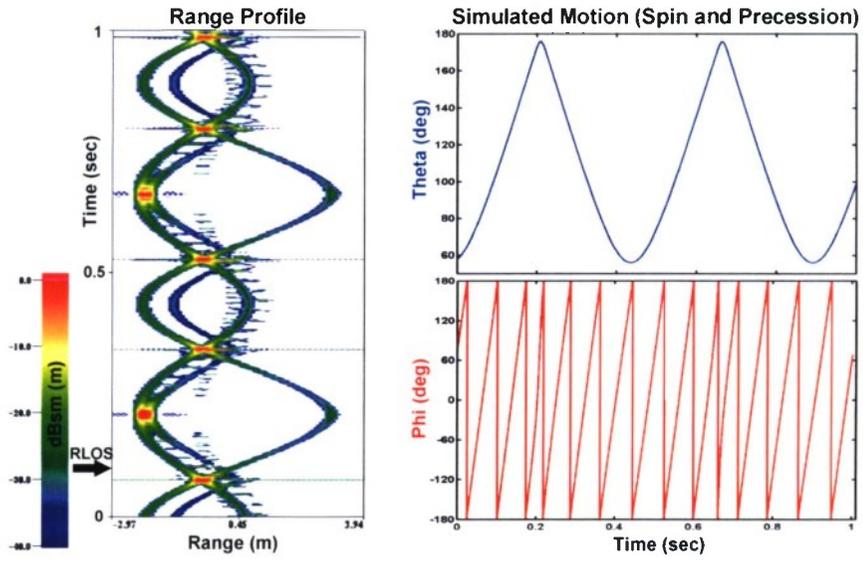
Figure 11. RTI Plot of Simulated Rocket Body
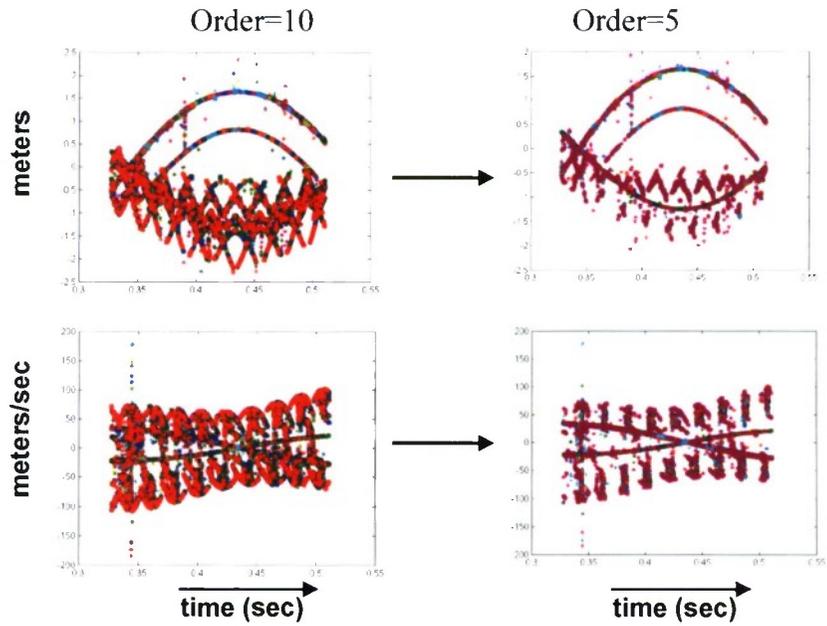
*Figure 12. (Rn,Rnd Sequence vs. Time)*

Over this time interval, the sequence $\left\{R_n, \dot{R}_n, D_n\right\}_{t=t_1,\ldots,t_q}$ provides a comprehensive representation of the field scattered from the target. In applying the spectral estimation algorithm to each data block, typically one assumes an order, N, of the number of scatterers characterizing the target. Generally one chooses N-large and then filters the result by thresholding on the amplitude, $|D_n|$.
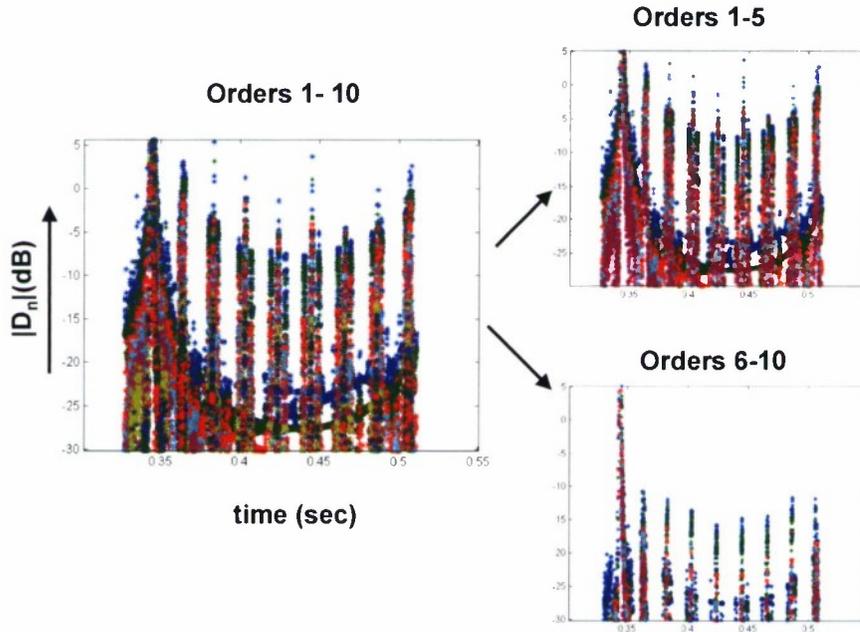

Figure 13. Scattering Amplitudes (dB)

In Figure 12 we illustrate the $\left(R_n, \dot{R}_n\right)$ sequence assuming N = 10, and then threshold the result for the five dominant centers indicated by order = 5 on the figures. The corresponding $|D_n|$ (in dB) are indicated in Figure 13. Noting the nearly 20-dB reduction in lower order poles, we use only the dominant five poles for the following simulation.

As discussed in detail in Reference 1, a key advantage of the "snapshot imaging" technique is that when contrasted to other Extended Coherent Processing (ECP) techniques, only a limited set of snapshots are required to characterize the target. Thus, once a specific scattering center is identified and located on the target, additional data does not add significantly to the location estimate. (Other than for noisy data, where additional data increases the effective SNR) For our purposes, to illustrate the methodology developed in Section 6, we choose a subset of $\left(R_n, \dot{R}_n\right)$ data over the time interval (0.43, 0.47) seconds.

27

Over this interval, the target aspect is nearly constant at $\theta \sim 60°$, $|\dot\theta| \ll |\dot\phi|$ and the spinning motion of the target dominates. This localized motion, in effect, looks like a spinning target at constant aspect angle. Figure 14 illustrates the $\left(R_n, \dot R_n\right)$, n=1,...,5, sequence over this interval (vs. sequence label q, where $t = t_1,...t_q$. and q ranges from (1 − 4533) over the (0.43, 0.47) time interval chosen. We also plot the (θ, ϕ) variation over this data set interval. As discussed, θ is nearly constant at 60° and ϕ ranges over a roughly 190° interval (115° − 305) degrees.
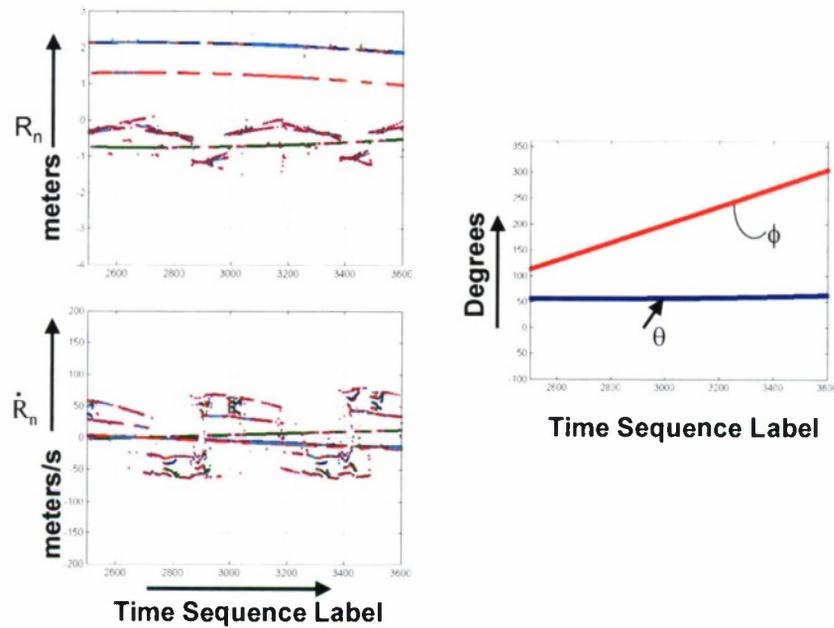

Figure 14. $\left(R_n, \dot R_n\right)$ *and* θ, ϕ *Used for Imaging Simulation*

Figure 15 illustrates the results of applying the surface constraint imaging algorithm to a small data subset of 275 angle steps, over which ϕ ranges over a 47° sector, and this sector is moved progressively through 190° to cover one-half of target revolution. The scattering centers detected are plotted in "red" overlaid on the "green" surface model. As expected, dominant scattering occurs from the cylinder edges and the fins. Most interestingly, the scattering from each of the two visible fins indicates that significant scattering occurs from all parts of the fins. Also note that the location of the point scatter contributions is consistent with incident angle. Figures 15b), c) and d) continues the sliding 47° sector image sequence, progressively showing how differing scattering centers appear on the target as the target rotates.

$\phi = (113, 160)$ Deg $\phi = (160°, 207)$ Deg

$\phi = (254°, 301°)$ Deg $\phi = (207, 254°)$ Deg
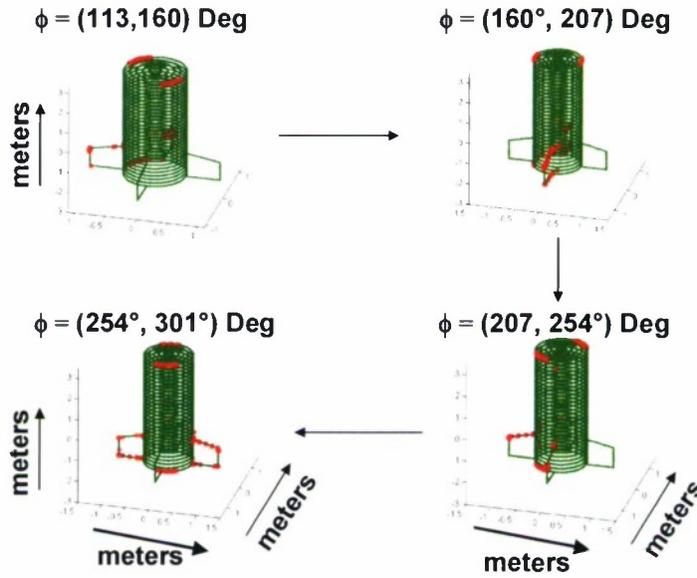
Figure 15. Sequential 47-deg Sector Images

Finally, we illustrate in Figure 16 the composite of the images in Figure 15 – i.e. ϕ ranges over the full interval (113° – 301°). We show a 3D view as well as top and side views. Observe that we do pick up a few stray false scattering points. These however result from the output of the spectral estimation algorithm (See Figure 12) as sometimes "glitch points" occur. We have yet to perfect this algorithm to eliminate these points. They could readily be filtered out, however, using a "noise filter" in series with the ambiguity filters.

Careful examination of the scattering centers extracted from Figure 16 indicates that a component-based signature model of this target can be constructed using only the fin-components and three slipping scatterers: the visible truncated cylinder forward and rear slipping scatterers and a slipping scatterer at the visible rear base of the cylinder. The coefficient D_n (θ, ϕ) for each of these components is readily determined from the extracted pole complex amplitudes (see Figure 13), and the scattered field can be reconstructed by superposition of field scattered from each of these scattering components.

Top View

Side View

3D View
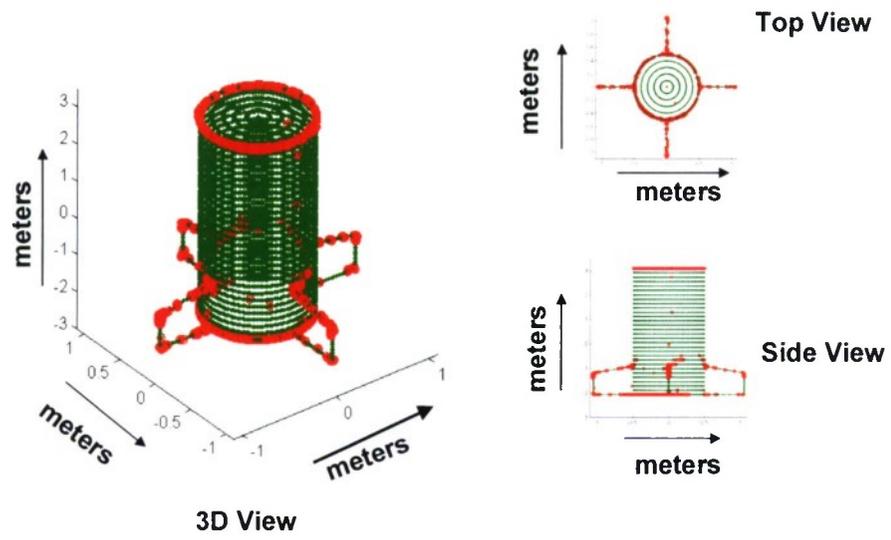
Figure 16. Composite Image Points Over 190° Spin Angle

8. SUMMARY

In this paper, we extend the novel formulation for 3D imaging of ISAR data using recent developments in high-resolution spectral estimation theory to the situation where some apriori information about the target surface geometry is known.

For some applications one has apriori information about the target geometry – For example in processing static range data or in processing flight-test field data on known targets. Of prime interest in this case is identification of the dominant scattering centers on the target, with the intent to form a computationally efficient, measurements based, signature model of the target. In this report, we develop a methodology which incorporates this known surface geometry constraint to generate a 3D ISAR image identifying the principal scatterers contributing to the target radar cross-section. The methodology uses only a sequence of single snapshots of data from which key features on the target can be readily extracted. The technique eliminates the need for a range-Doppler correlator required to track any specific scatterer. This is accomplished by hypothesizing a given target surface constraint (3D), and mapping sequential 2D range-Doppler location estimates onto this surface. The process is adaptive, as the assumed geometry is modified as appropriate to fit the data. When applied to the sequence of high-resolution snapshots obtained using the direct spectral estimate obtained from sequential blocks of data, it presents a computationally efficient way of generating a high-resolution 3D image where the dominant scattering centers on the given surface constraint are identified and characterized.

We have presented several examples, which illustrate the utility of the technique. Two generic shapes, a cone and a cylinder, allow for an analytic solution leading to a quadratic equation characterizing the scatterer locations. The two roots obtained from the quadratic correspond to a true scatterer location, and an ambiguous solution that must be filtered out. We consider four physical mechanisms for these ambiguity filters: shadowing; slipping scatterers; component-to-component coupling and CAD model surface tolerances. The latter two are applicable to the case considered where we apply a more general surface constraint characterized by Eq (32). We illustrate these filters applied to a more complex target geometry consisting of a finite cylinder having four equally spaced fins at the rear.

Applications of the technique illustrate the snapshot nature of the component extraction – i.e. one not need a continuous wide-angle sector of data to generate a 3D image. Thus it is particularly applicable to 3D imaging of sectors of sparse-angle data.

The extracted scattering locations (x_n, y_n, z_n) and component features (i.e., $|D_n|$ vs. angle) can be used to develop a computationally efficient, measurements-based RCS signature prediction model. A key attribute of the resulting model is that the measured RCS is directly incorporated into the computational model. The extracted scattering locations and component features can be combined using the Geometrical Theory of Diffraction (GTD) to reconstruct the scattered field in the data observation region (see Eq (2)), and using physics-based characterization of the components, extrapolated outside the observation region for wide-angle characterization of the target RCS.

REFERENCES

1.   Mayhan, J.T. Burrows, M.L., Cuomo, K.M., Piou, J.E., "High-resolution 3D Snapshot ISAR Imaging and Feature Extraction," IEEE Transactions on Aerospace and Electronic Systems, AES-37, 630-641, April, 2001.

2.   J. B. Keller, "Backscattering from a Finite Cone," IEEE Trans. On Ant. & Prop., March, 1960 (pp 175-182).

3.   Burrows, M.L., "Two Dimensional ESPRIT with Tracking for Radar Imaging and Feature Extraction," MIT Lincoln Laboratory Technical Note, No. 1084, 2 August 2002.

4.   K. M. Cuomo, J. E. Piou and J. T. Mayhan, "Ultrawideband Coherent Processing," IEEE Trans. Antennas & Prop., 47, 1094-1107 (1999).

5.   L. D. Vann, K. M. Cuomo, J. E. Piou and J. T. Mayhan, "Multi-Sensor Fusion Processing for Enhanced Radar Imaging," LL Technical Report, TR-1056.

REPORT DOCUMENTATION PAGE		Form Approved OMB No. 0704-0188

The public reporting burden for this collection of Information is estimated to average 1 hour per response, including the time for reviewing instructions, searching existing data sources, gathering end maintaining the data needed, and completing and reviewing the collection of information. Send comments regarding this burden estimate or any other aspect of this collection of Information, including suggestions for reducing the burden, to Department of Defense, Washington Headquarters Services, Directorate for Information Operations and Reports (0704-0188), 1215 Jefferson Davis Highway, Suite 1204, Arlington, VA 22202-4302. Respondents should be aware that notwithstanding any other provision of law, no person shall be subject to eny penalty for falling to comply with e collection of information if it does not display a currently valid OMB control number.
PLEASE DO NOT RETURN YOUR FORM TO THE ABOVE ADDRESS.

1. REPORT DATE *(DD-MM-YYYY)*	2. REPORT TYPE	3. DATES COVERED *(From - To)*
23 March 2004	Technical Report	

4. TITLE AND SUBTITLE	5a. CONTRACT NUMBER
RCS Scatterer Extraction Using Apriori Target Information	F19628-00-C-0002
	5b. GRANT NUMBER
	5c. PROGRAM ELEMENT NUMBER

6. AUTHOR(S)	5d. PROJECT NUMBER
J.T. Mayhan	
	5e. TASK NUMBER
	5f. WORK UNIT NUMBER

7. PERFORMING ORGANIZATION NAME(S) AND ADDRESS(ES)	8. PERFORMING ORGANIZATION REPORT NUMBER
Lincoln Laboratory, MIT 244 Wood Street Lexington, MA 02420-9108	TR-1093

9. SPONSORING/MONITORING AGENCY NAME(S) AND ADDRESS(ES)	10. SPONSOR/MONITOR'S ACRONYM(S)
Space and Missile Defense Technical Center P.O. Box 1500 Huntsville, AL 35807	USASMDTC/SMDC-TC-MT-E
	11. SPONSOR/MONITOR'S REPORT NUMBER(S)
	ESC-TR-2003-078

12. DISTRIBUTION/AVAILABILITY STATEMENT

Approved for public release; distribution is unlimited.

13. SUPPLEMENTARY NOTES

None

14. ABSTRACT

An essential ingredient in forming a measurements-based signature model valid over a wide range of frequencies and angles is the ability to map the field measurement data (2 dimensional) onto a component-based three-dimensional (3D) geometry. To accomplish this, 3D characterization of the target scattering components is required. Typically, this 3D characterization of the scatterer locations is obtained by forming a 3D image of the target, and extracting the dominant scattering centers. In this paper we extend the novel formulation for 3D radar imaging of Inverse Synthetic Aperture Radar (ISAR) sparse-angle data using high-resolution spectral estimation theory presented in a previous paper (Ref 2) to the special case where one has apriori information about the target geometry.

15. SUBJECT TERMS

ISAR Imaging, Target Identification, RCS Components, BMD Target Characterization

16. SECURITY CLASSIFICATION OF:			17. LIMITATION OF ABSTRACT	18. NUMBER OF PAGES	19a. NAME OF RESPONSIBLE PERSON
a. REPORT	b. ABSTRACT	c. THIS PAGE	Same as Report	40	
U	U	U			**19b. TELEPHONE NUMBER** *(Include area code)*

Standard Form 29B (Rev. 8/9B)
Prescribed by ANSI Std. Z39.18